BNL-73602-2005-IR

BROOKHAVEN
NATIONAL LABORATORY

Self-assembly Ce oxide/Organopolysiloxane Composite Coatings

T. Sugama

R. Sabatini
Materials Science Department

K. Gawlik
National Renewable Energy Laboratory
1617 Cole Boulevard
Golden, CO 80401

January 2005

Energy Sciences and Technology Department
Energy Resources Division

Brookhaven National Laboratory
P.O. Box 5000
Upton, NY 11973-5000
www.bnl.gov

Managed by
Brookhaven Science Associates, LLC

This program report, issued by DOE Office of Geothermal Technologies, was performed under the auspices of the U.S. Department of Energy, Washington, D.C. under Contract No. DE-AC02-98CH10886

DISCLAIMER

Abstract

A self-assembly composite synthesis technology was used to put together a $Ce(OH)_3$-dispersed poly-acetamide-acetoxyl methyl-propylsiloxane (PAAMPA) organometallic polymer. Three spontaneous reactions were involved; condensation, amidation, and acetoxylation, between the Ce acetate and aminopropylsilane triol (APST) at 150°C. An increase in temperature to 200°C led to the *in-situ* phase transformation of $Ce(OH)_3$ into Ce_2O_3 in the PAAMPA matrix. A further increase to 250°C caused oxidative degradation of the PAAMPA, thereby generating copious fissures in the composite. We assessed the potential of $Ce(OH)_3$/ and Ce_2O_3/ PAAMPA composite materials as corrosion-preventing coatings for carbon steel and aluminum. The Ce_2O_3 composite coating displayed better performance in protecting both metals against NaCl-caused corrosion than did the $Ce(OH)_3$ composite. Using this coating formed at 200°C, we demonstrated that the following four factors played an essential role in further mitigating the corrosion of the metals: First was a minimum susceptibility of coating's surface to moisture; second was an enhanced densification of the coating layer; third was the retardation of the cathodic oxygen reduction reaction at the metal's corrosion sites due to the deposition of Ce_2O_3 as a passive film over the metal's surface; and, fourth was its good adherence to metals. The last two factors contributed to minimizing the cathodic delamination of coating film from the metal's surface. We also noted that the affinity of the composite with the surface of aluminum was much stronger than that with steel. Correspondingly, the rate of corrosion of aluminum was reduced as much as two orders of magnitude by a nanoscale thick coating. In contrast, its ability to reduce the corrosion rate of steel was lower than one order of magnitude.

1. Introduction

With increased demand for selling electricity in geothermal binary plants during the most valuable summer season, one very important issue is the impairment of the efficiency of the air-cooled condensers, thereby causing ~ 30 % reduction in the plant's net monthly energy delivery compared with that in the winter [1]. A simple method to deal with this problem is to directly spray inexpensive relatively clean cooled geothermal brine over the surfaces of the aluminum-finned steel condenser tubes [2]. As expected, such sprayed condensers then attain outputted the same generating capacity for electricity as under wintertime conditions. Although this method is very attractive, a concern raised about spraying the brine is the likelihood of corroding the condenser's components, aluminum fins and carbon steel tubes, as well as depositing geothermal brine-induced mineral scales such as silica and calcium carbonate on these components. There is no doubt that such negative phenomena, corrosion and scale deposit, are detrimental to retaining the condenser's function and efficacy [3].

The polyaminoproplysiloxane (PAPS) polymer was previously synthesized by the heat-catalyzed condensation reactions of a water-based aminopropylsilane triol (APST) precursor solution that possesses great penetrating and wicking behaviors moving readily through spaces between the fins of less than 3 mm. We then evaluated its potential as an anti-corrosion coating for the condensers [4]. With PAPS films of up to 2.2 μm thick, their excellent adherence to the surfaces of aluminum fins offered an outstanding protection against brine-caused corrosion. For instance, the useful lifetime of bare aluminum exposed in a 15 % salt-fog chamber at 35°C was considerably extended from only ~ 40 hours to more than 1400 hours by depositing the PAPS coating on its surfaces. In contrast, when this coating was applied to carbon steel, its effectiveness in mitigating corrosion was much less; the useful lifetime of bare steel was extended from ~ 10 hours to only ~ 216 hours.

Thus, our attention focused on improving the corrosion-preventing performance of PAPS coating, in particular for carbon steel. The factors to be improved included: One was the transformation of functional amine end groups within PAPS into the hydrophobic

amid groups, and the other was to incorporate the cerium (Ce) hydroxide and oxide as corrosion inhibitor in the coating. The former factor will contribute to improving water-shedding and –repellent properties of the coating's surface, which is one of inevitable properties as a water-impermeable, corrosion-mitigating barrier layer. For the latter factor, among the rare-earth metal salts, the environmentally benign Ce salt compounds displayed high potential as a promising alternative corrosion inhibitor for replacing the toxic hexavalent chromium (Cr^{6+}) salt compounds used both as a pigment in the polymer coatings, and as the conversion coating in anodizing baths [5-11]. In our previous study on enhancing the ability of poly(D-glucosamine) biopolymer coating to protect aluminum against the corrosion [12], we found that the amine group in poly(D-glucosamine) favorably reacted with the butyryloxy group in the dihydroxy butyryloxy Ce intermediate to form the hydrophobic amide group, and also to simultaneously disperse the cerium hydroxide in the coating layer. Adapting this synthetic technology that made it possible to yield spontaneously the amide group and Ce hydroxide in the polymeric matrix, the Ce acetate was opted for this study from among the Ce-based salt compounds.

Based upon information described above, the objective in this study was to investigate the characteristics of an upgraded organopolysiloxane-based polymer coating derived from the Ce acetate-modified APST precursor solution as a corrosion-preventing coating for both aluminum and carbon steel substrates. Most of our attention was directed towards corrosion, rather than to scale deposition and its prevention. A film with more than ~ 2.2 μm thick was applied to these substrates because a thinner layer thickness was not adequate to protect the carbon steel. In addition, three different baking temperatures, 150°, 200°, and 250°C, for the precursor-wetted substrates were adapted to obtain information on the best film-forming performance, in conjunction with the ideal chemical structure responsible for the most promising corrosion protection. The several characteristics investigated included the following: The wetting and spreading behaviors of the Ce acetate-modified APST precursor solution over the aluminum and steel surfaces; the changes in polymer structure and the phase transformation of the Ce compound as a function of baking temperature; its water repellency; and, the

morphological alterations on the film's surface at an elevated baking temperature. All the data were integrated and correlated directly with information obtained from the corrosion-related studies, including impedance spectroscopy, potentiodynamic polarization, and salt-spraying resistance.

2. Experimental

2.1. Materials

Aminopropylsilane triol [H_2N-$(CH_2)_3$-$Si(OH)_3$, APST] (25wt % in water), supplied by Gelest, Inc., was used as a network-forming monomeric organosilane precursor. The cerium (Ce, III) acetate hydrate, $(CH_3CO_2)_3Ce.xH_2O$, as the corrosion-inhibiting dopant in the APST, was obtained from Aldrich. To prepare the Ce acetate-doped APST precursor solutions, 3.0wt% Ce acetate was added to the 25 wt% APST solution. The metal substrates, supplied by Advanced Coating Technologies, Inc., were 3003 aluminum (Al), and AISI 1008 carbon steel test panels.

2.2. Coating method

The surfaces of these substrates were coated with the non-doped and doped APST precursor solutions in the following sequence. First, to remove any surface contaminants, the test panels were immersed for 20 min at 80°C in an alkaline solution consisting of 0.4 wt% NaOH, 2.8 wt% tetrasodium pyrophosphate, 2.8 wt% sodium bicarbonate, and 94.0 wt% water. The alkali-cleaned panels were washed with deionized water at 25°C for 1 min, and dried for 15 min at 100°C. Then, the panels were dipped into a soaking bath of precursor solutions at room temperature, and withdrawn slowly. The wetted substrates were left for 20 hours in an atmospheric environment at room temperature to convert the precursor solution into a gelled film. All the gelled films then were baked in an air oven for 120 min at 150°C to yield solid films. Some 150°C- baked films were further heated for 120 min at 200° or 250°C.

2.3. Measurements

The surface tension of doped APST solutions was determined with a Cenco-DuNouy Tensiometer Model 70535. The thickness of coating films deposited on the metal substrates was measured with the Dektak Surface Profile Measurement. Using a contact angle analyzer (Model CAA-3, Imass Instruments), the extent of wettability and spreadability of the non-doped and Ce acetate-doped APST solutions over the aluminum and steel surfaces was determined by measuring the contact angle within the first 30 sec. after dropping the solution onto the metal surfaces. Similar measurements were made of the contact angle to evaluate the susceptibility to moisture of the solid film's surfaces derived from the non-doped and doped APST solutions. In this case, the changes in the contact angle were made by dropping water onto the surfaces of the coating films, and its angle was measured within 30 sec. Fourier Transform Infrared (FT-IR, Model 1600, Perkin Elmer) was employed to obtain the information on the changes in the polymer structure of the solid film and the phase transformation of the Ce compound that was yielded as the reaction byproduct as a function of baking temperature. This information also was supported by thermogravimetric analyzer (TGA, Model 951, TA Instruments) and X-ray photoelectron spectroscopy (XPS, Model CLAM 100, VG Scientific Ltd). Scanning electron microscopy (SEM) coupled with energy-dispersive x-ray spectrometry (EDX) was used to explore the morphological alterations of the film's surface as a function of baking temperature. The extent of ionic conductivity of electrolyte through the coating films deposited on the steel was determined by AC electrochemical impedance spectroscopy (EIS). Specimens with a surface area of 13 cm^2 were exposed to an aerated 0.5 M sodium chloride electrolyte at 25°C, and single-sine technology with an input AC voltage of 10 mV (rms) was employed over a frequency range of 10 KHz to 10^{-2} Hz. To estimate the protective performance of the coatings, the pore resistance, Rp, (ohm-cm^2) was determined from the plateau in Bode-plot scans that occurred in low frequency regions. DC electrochemical testing for corrosion was performed with the EG&G Princeton Applied Research Model 362-1 Corrosion Measurement System. The electrolyte was a 0.5 M sodium chloride. The specimen was mounted in a holder, and

then inserted into an EG&G Model K47 electrochemical cell. The test was conducted under aerated conditions at 25°C, on an exposed surface area of 1.0 cm^2. The polarization curves were measured at a scan rate of 0.5 mVs^{-1} in the corrosion potential range from -1.35 to -0.75 V. The salt-spray tests of the coated aluminum and carbon steel panels (75 mm x 75 mm, size) were preformed in accordance with ASTM B 117, using a 5 wt% NaCl solution at 35°C.

3. Results and discussion

3.1. Properties of precursor solutions

Table 1 shows the pH value, surface tension, and contact angle over the cleaned aluminum and carbon steel surfaces for Ce acetate-modified and unmodified APST precursor solutions. The pH value of the unmodified solution fell slightly from 10.95 to 10.54 as 3wt% Ce acetate was added. The surface tension of unmodified solution increased by 2 % to 56.2 dynes/cm when Ce acetate was incorporated. As expected, the increase in the surface tension of the solutions corresponded to the increase in the value of contact angle, θ, of solutions dropped on the surfaces of aluminum and carbon steel, demonstrating that the solution with high surface tension exhibited poor wetting behavior on these metal surfaces. In fact, when a droplet of the modified solution with a higher surface tension than that of the unmodified one impinged on the these metal surfaces, its contact angle for steel and aluminum rose 3.7 % and 8.6 % to 42.3° and 29.2°, respectively. Also, the data revealed that both the modified or unmodified solutions show much better wettability on aluminum surfaces than on steel surfaces, reflecting this finding that the θ value on aluminum can be reduced by as much as 1.5 fold compared with that of steel.

3.2. Chemical Structures of Solid Films

As described in the coating technology section, thermal temperatures of ≥ 150°C were required to convert the precursor solution into a solid film. Thus, of particular interest was the change in chemical structure within the solid films in the temperature

range of 150° to 250°C. To obtain this information, we investigated the FT-IR spectra of the solid films made by heating the unmodified and Ce acetate-modified APST solutions at 150°, 200°, or 250°C. The spectra were run over the frequency range from 2000 to 500 cm^{-1}. Figure 1 gives the FT-IR spectra for unmodified films. The spectrum of the 150°C film included eight absorption bands: according to the literature [13,14], those at 1660 and 1600 cm^{-1} are attributable to the N-H bending vibration in the NH_2 group; that at 1443 cm^{-1} reveals CH_2 stretching vibration in the propyl groups; at 1126 the band can be ascribed to the stretching mode of the Si-C bond in the Si-joined propyl groups; that at 1031 cm^{-1} is believed to originate from the antisymmetric bond stretching of the oxygen-bridged Si-O-Si linkage in the polysiloxane structure; at 930 cm^{-1} that band corresponds to the Si-O stretching mode of non-bridging oxygen in the Si-OH silanol groups; while those at 780 and 691 cm^{-1} are associated with the symmetric stretching and bending modes, respectively, of the Si-O-Si linkage. These data clearly revealed that during the transformation of the APST solution into a solid film at 150°C, dehydrating condensation reactions between the silanol groups within the APST create a polysiloxan structure represented by the formation of the Si-O-Si linkages, ≡Si-OH + HO-Si≡ → ≡Si-O-Si≡ + H_2O. Thus, the solid films of polyaminopropylsiloxane (PAPS) polymer had the following chemical network structure:

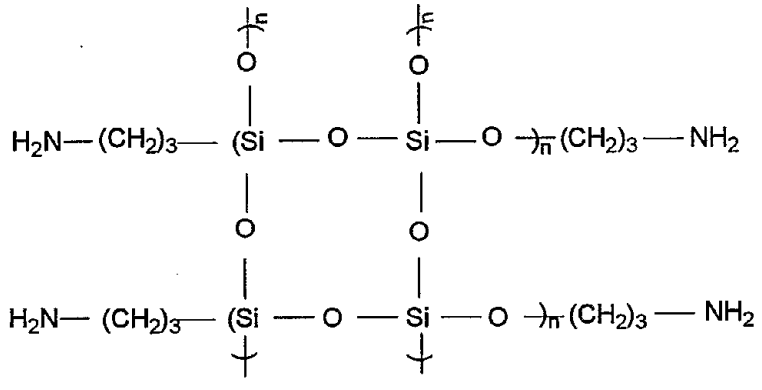

Also, we believe that because of the presence of a noticeable band at 930 cm^{-1}, some non-reacted silanol groups still remained in the PAPS polymer made at 150°C.

Increasing the temperature to 200°C caused three conspicuous changes in the spectral features compared with that of the150°C film: First was a striking decrease in the

absorbance at 1600 cm^{-1}, which is one of the NH_2-related bands; second was that the intensity of Si-C bond-related band at 1126 cm^{-1} became weaker than that of the Si-O-Si linkage band at 11031 cm^{-1}; and, third was the conversion of the silanol-related peak at 930 cm^{-1} into a shoulder peak, reflecting a decrease in number of non-reacted silanol groups. The possible interpretation for the decline in silanol groups was that 200°C promoted condensation reactions between the non-reacted silanol groups remaining in the 150°C polymer. At 250°C, the film's spectral features were quite different from that of the 200°C film; in particular, the new band appearing at 1719 cm^{-1} was attributed to the carbonyl (C=O) group in aldehyde (-CHO), ketone (C-O-C), and carboxylic acid (-COOH) as oxidation reaction products along with the nearly complete elimination of the CH_2-associated band at 1443 cm^{-1}, and also the Si-C band at 1126 cm^{-1} had become a shoulder peak. This finding strongly suggested that on baking the film at 250°C, it underwent oxidation degradation; namely, two bonds, C-H and Si-C, in the Si-joined propyl groups, were vulnerable to the reaction with oxygen to form aldehyde, ketone, and carboxylic acid as oxidative derivatives.

To support this information, we inspected by XPS the O/C atomic ratio and C_{1s} core-level spectra excited at the outermost surface site of 150°, 200°, and 250°C-baked PAPS films. The O/C atomic ratio was obtained by comparing the XPS O_{1s} and C_{1s} peak areas, which then were converted into atomic fractions. All XPS measurements were made at an electron take-off angle of 45°, corresponding to an electron-penetration depth of ~ 5.0 nm. Figure 2 depicts the changes in the atomic ratio of O/C for the PAPS film surfaces as a function of baking temperature. The value of O/C ratio of the 150°C-baked PAPS was 0.42; This it rose by ~ 21 % to 0.51 as the temperature increased to 200°C. A further increase to 250°C raised it conspicuously by as much as 1.9 fold higher than that at 150°C. These findings were compelling evidence that a meaningful amount of oxygen was incorporated into the film's surface at 250°C. In other words, baking at 250°C resulted in a higher degree of the oxidation of film, than at 150° and 200°C.

Figure 3 compares the XPS C_{1s} core-level photoemission spectra of the films' surfaces baked at 150°, 200°, and 250°C. A curve deconvolution technique was employed

to substantiate the information on the carbon-related chemical states from the spectrum of the carbon atom. The spectrum at 250°C can be deconvoluted by three resolvable Gaussian components at the binding energy (BE) positions of 285.0, 287.8, and 289.3 eV. The principal contributor to the major peak at 285.0 eV was due to the C of the $-CH_2-$ groups within the PAPS polymer. The remaining two excitation peaks at 287.8 and 289.3 eV as the minor components are originated from the C in the C=O and COOH groups as the oxidative derivatives, respectively. The C=O group can be associated with either aldehyde or ketone. Compared with that of the PAPS made at 250°C, the overall spectral feature at 200°C was characterized by representing a striking decay of the minor peaks at 287.8 and 289.3 eV, while showing stronger excitation of the $-CH_2-$ associated major peak. Further attenuation of the excitation of these two minor peaks was seen in PAPS made at 150°C. Although there is some oxidation in the films at 200° and 150°C, its degree might be little, if any. Thus, these XPS data strongly upheld the results from the FT-IR study; namely, the-CH_2- in the Si-joined propyl groups underwent oxidation degradation to form three oxidative derivatives, aldehyde, ketone, and carboxylic acid, thereby leading to the formation of a radical due to the rupture of the bond between Si and C;

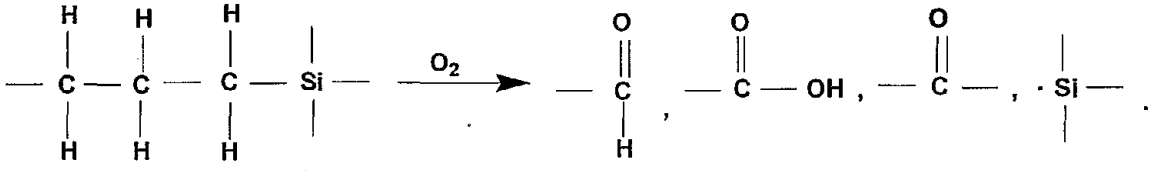

Figure 4 illustrates the FT-IR spectra for the films derived from the Ce acetate-modified APST solutions at 150°, 200°, and250°C. At 150°C, four additional bands at 1658, 1554, 1384, and 1302 cm^{-1} appeared in the spectrum, compared with that of a film from the unmodified APST at the same temperature (see figure 1). Among those additional bands, the 1658, 1554, and 1302 cm^{-1} frequencies are ascribed to the stretching

mode of C-N bond in the amide group, -CO-NH-R [15] as the reaction product. Regarding the remaining new band at 1384 cm^{-1}, we thought that this band might include two reaction products: One is the symmetric bending mode of acetoxyl methyl group linked to the Si element, Si-O-CO-CH_3 [16]; and the other is related to the Ce^{3+} hydroxide. For latter reaction product, we inspected by FT-IR the two Ce-related compounds, Ce hydroxide and Ce oxide, as reference samples (Figure 5). As seen, Ce hydroxide had a pronounced band at 1384 cm^{-1}. In contrast, there was no such peak for Ce oxide. Thus, the major contributor to the band at 1384 cm^{-1} is Ce hydroxide. Nevertheless, it is reasonable to rationalize that the amide group was formed by an amidation reaction between the amine group in APST and the Ce acetate: $Ce(\text{-O-}COCH_3)_3 + 3H_2N\text{-} \rightarrow 3CH_3CO\text{-NH-} + Ce(OH)_3$. This reaction also led to the formation of cerium hydroxide, $Ce(OH)_3$, as the reaction byproduct. On the other hand, the acetoxyl methyl group as the minor reaction product was derived through the acetoxylation reaction between the silanol in APST and Ce acetate along with the formation of $Ce(OH)_3$: $Ce(\text{-O-}COCH_3)_3 + 3{\equiv}Si\text{-OH} \rightarrow 3CH_3CO\text{-O-Si}{\equiv} + Ce(OH)_3$, underscoring that Ce acetate has a chemical affinity for two groups in APST, amine and silanol. Consequently, we represent below the hypothetical conformation of polymer derived from Ce acetate-modified APST; it is categorized as a poly-acetamide-acetoxyl methyl-propylsiloxane (PAAMPS) polymer.

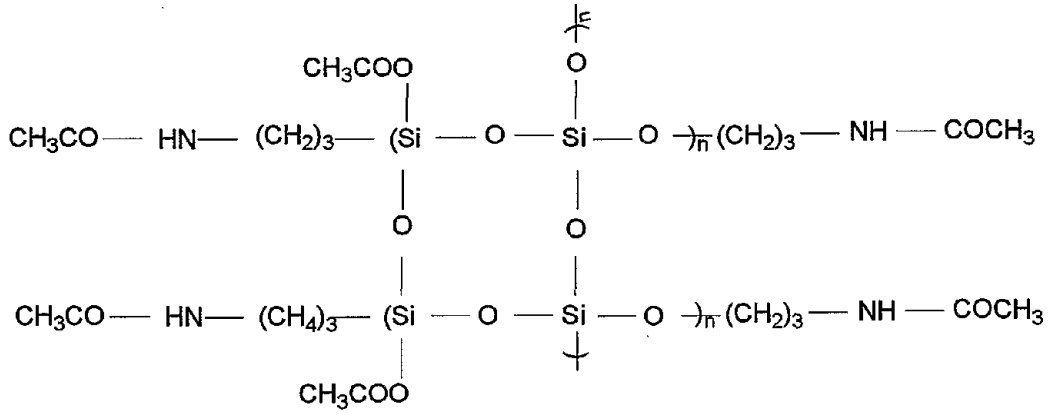

Returning to the figure 4, the spectral feature of 200°C-baked film somewhat differed from that of the 150°C film, especially as follows: (1) the disappearance of band at 1600 cm^{-1} attributed to the non-reacted NH_2 group, (2) a considerable reduction in the intensity of 1384 cm^{-1} band, related to the $Ce(OH)_3$ and acetoxyl methyl group as the major and minor reaction products, respectively, (3) a less intense Si-C bond-related band at 1126 cm^{-1} compared to that of the Si-O-Si linkage-associated band at 1031 cm^{-1}, and (4) a marked decrease in signal intensity of silanol group-related band at 930 cm^{-1}. The differences (1), (3), and (4), also were observed from that of the unmodified film at the same temperature. Regarding the item (2), the pronounced decrease in band's intensity at 1384 cm^{-1} is more likely to be associated with the *in-situ* transformation of Ce hydroxide into the Ce oxide phase by dehydration at 200°C, rather than the decomposition of acetoxyl methyl group. Assuming that such a hydroxide → oxide transformation took place in the film, an intriguing question centers on what type of valence states of oxide can be formed, Ce^{3+} or Ce^{4+}, or both. To gain this information, we surveyed the XPS Ce_{3d} core-level spectrum of the 200°C-made PAAMPS film's surface (Figure 6). The two peaks at 885.5 eV in $3d^{5/2}$ region and at 904.2 eV in $3d^{3/2}$ region can be attributed to the formation of Ce^{3+} oxide, Ce_2O_3, [17, 18], but not to the Ce^{4+} oxide, CeO_2, because of the absence of satellite peak near 916 eV. A similar spectral feature also was observed from the 150°C film's surface (not shown). Correspondingly, upon heating the film at 150°C, Ce^{3+} hydroxide, $Ce(OH)_3$, was formed in the film, and later transformed into the Ce_2O_3 by its dehydration at 200°C; $2Ce(OH)_3 \rightarrow Ce_2O_3 + 3H_2O$. At 250°C, like the unmodified PAPS film, the PAAMPA polymer also underwent the oxidation; in particular, the Si-joined propyl group within this polymer structure again was targeted for oxidative degradation. Subsequently, the spectrum showed three oxidation-related changes; (1) the appearance of new band at 1719 cm^{-1} that originated from the C=O groups in the aldehyde, ketone, and carboxylic acid oxidative derivatives, (2) a considerable reduction in the intensity of the band at 1443 cm^{-1} associated with the $-CH_2-$ in the propyl group, and (3) the alteration in the shape of the band representing the Si-C bond at 1126 cm^{-1} to a shoulder band.

To substantiate thermal dehydration process of $Ce(OH)_3$ at 200°C, we conducted a TGA study of the 150°, 200°, and 250°C-made PAAMPA films. Figure 7 depicts their TGA curves over the range of 80° and 800°C. The curve for the 150°C film revealed two pronounced decomposition states; the first began at the onset temperature near 200°C, and the second as the primary phase of decomposition, occurred around 360°C. In the first state, the weight loss of ~ 3.5 % occurring between 200° and 315°C reflects the thermal dehydration of $Ce(OH)_3$. The second state related to the major weight loss of ~ 30.5 % occurred between 360° and 650°C, and was due to the thermal decomposition of PAAMPA polymer. In contrast, there was no sign of the decomposition beginning around 200°C in the curves of the 200° and 250°C films, nor, indeed, any signs until major decomposition took place at ~ 360°C, almost the same onset temperature as that of the 150° film. Hence, this finding clearly manifests that amidation-acetoxylation reactions between Ce acetate and APST at 150°C led to the formation of $Ce(OH)_3$, which then underwent dehydration at 200°C, converting it into Ce_2O_3. The data also showed that although all the PAAMPA films (150°, 200°, and 250°C) exhibited major decomposition at ~ 360°C, their total loss in weight at 800°C depended on the baking temperatures. For instance, the total weight loss at 800°C of the 250°C-baked film was ~ 20 %, corresponding to as much as 45 % lower than that of the 150°C film at the same temperature, meaning that some volatile organic oxidative derivatives were yielded at 250°C, and emanated from the film during baking. Such a volatilization of oxidative derivatives may be detrimental to creating a uniform, fissure-free coating because of the generation of some shrinkage in the film.

Nonetheless, the integrated information from the above FT-IR, XPS, and TGA studies verified that three spontaneous reactions, condensation, amidation, and acetoxylation, between the Ce acetate and APST at 150°led to the formation of the composite structure consisting of the PAAMPA as polymer matrix and $Ce(OH)_3$ as the filler. However, some non-reacted silanol groups remained in this film. Increasing the

temperature to 200°C promoted condensation reactions between these non-reacted silanol groups to form an additional polysiloxan network structure.

3.3. Film-forming Performance

To visualize how seriously the oxidation of the PAAMPA polymer affects the film-forming performance on the substrate's surface, the changes in morphology of the coatings' surfaces deposited on the carbon steels' surfaces as a function of baking temperature was explored by SEM (Figure 8). The SEM images revealed that baking temperatures at 150° and 200°C offered a great film-forming performance because of the structure of the fissure–free continuous film presenting a smooth surface texture. By contrast, at 250°C, the film developed copious cracks, underscoring that excessive oxidation of polymer was detrimental to fabricating an ideal uniform film. The same images (not shown) were obtained from the PAPS coating; namely, increasing the temperature to 250°C caused the development of cracks.

In preparing water-repellent and –shedding coating films, the susceptibility of the coatings' surfaces to moisture is among the important properties governing a good corrosion-preventing performance. Thus, our attention next focused on estimating the degree of water wettability of the PAPS and the PAAMPA/$Ce(OH)_3$ or /Ce_2O_3 composite coatings' surfaces made at 150°, 200°, and 250°C from the average value of the contact angle of a water droplet on their surfaces. Figure 9 plots the contact angle, θ, (deg) versus the baking temperature. At 150°C, the surfaces of the PAPS coating had θ values of 18.3°. The θ value of the $Ce(OH)_3$-filled PAAMPA composite was 50.5°, which was more than 2.7 fold as high as that of the PAPS, verifying that the composite coating's surface was mush less susceptible to moisture than that of the PAPS. Relating this finding to the early results from the FT-IR study, we can reasonably rationalize that this coating's moisture-insensitive surface is due to the presence of hydrophobic amide and acetoxyl methyl groups. Increasing the temperature to 200°C enhanced the θ value for both coatings, to 42.3° for the PAPS and 57.1° for Ce_2O_3-filled PAAMPA. This enhancement can be taken as evidence that an additional hydrophobic polysiloxan

network structure was formed by the condensation reaction between the non-reacted hydrophilic silanol groups remaining in both coatings at 150°C. A further increase in temperature to 250°C was no longer as effective as was that of the increase to 200°C. The θ value for both coatings declined because multiple-fissures appeared in the coating brought about by severe oxidation.

3.4. Corrosion Protection

Based upon the above information, our study then turned to evaluating the ability of $Ce(OH)_3$- and Ce_2O_3-filled PAAMPA coatings to protect the aluminum and carbon steel substrates against corrosion. For this comparison, the PAPS coating was used as the control. Three factors were evaluated: (1) The ionic conductivity of coating layer; (2) the cathodic delamination of the coating from the substrate's surface at the cathodic corrosion site; and, (3) the rate of corrosion of the coated metal substrates. Ionic conductivity is correlated directly with the extent of the uptake of corrosive electrolytes by the coating. The second factor is governed by the extent of the adherence of coating to the substrates' surfaces, and by the extent of its vulnerability at the coating/substrate interfacial boundary region to the alkali dissolution due to the alkaline environment created by the oxygen reduction reaction, $2H_2O + O_2 + 4e^- \rightarrow 4OH^-$, at cathodic corrosion sits of substrates. The AC EIS test was used to measure the first two factors, and the DC potentiodynamic polarization diagram and ASTM salt-spraying tests were employed for assessing the remaining one. The thickness of all the coatings for the EIS test ranged from ~ 3.5 to ~ 3.9 μm. An alkali-cleaned 65 mm x 65 mm aluminum and steel panels were used in these tests.

3.4.1. Carbon Steel

Figure 10 compares the features of EIS Bode-plot curve [the absolute value of impedance $|Z|$ (ohm-cm^2) vs. frequency (Hz)] for the steel panels coated with the PAPS polymer baked at temperatures of 150°, 200°, and 250°C. On the overall curves, our attention was focused on the impedance value in terms of the pore resistance, Rp. This

can be determined from the peak in the Bode plot occurring at a sufficiently low frequency ranging from 10^{-1} and 10^{-2} Hz. For the 150°C-baked PAPS coating, the curve revealed the typical feature representing the cathodic delamination of coating, reflecting a sharp drop of the impedance value after reaching a peak of 2.1×10^{3} ohm-cm^2 as the Rp value at around 4×10^{-2} Hz to 8.3×10^{0} ohm-cm^2 at 1×10^{-2} Hz. In fact, we visually observed the elimination of the coating film from the steel's surface after testing. Conceivably, the PAPS coating at 150°C not only adhered poorly to the steel, but also underwent interfacial alkali dissolution by the attack of OH^- ions generated at cathodic corrosion site of steel. In contrast, the 200°C coating showed no cathodic delamination, and its Rp value was raised one order of magnitude to 2.7×10^{4} ohm-cm^2. Since the Rp value reflects the magnitude of ionic conductivity generated by the NaCl electrolyte passing through the coating layers, the increased Rp value signified that the coating layer had become densified, so reducing the uptake of NaCl electrolyte. Additionally, two pivotal elements of the coating improved; its adherence to the steel, and the resistance to interfacial alkali dissolution. Relating these findings to the results from FT-IR earlier, we believe that at 200°C an additional polysiloxane network structure formed through the condensation reaction between the non-reacted silanol groups remaining in the coating at 150°C, and this played an important role in further densifing the coating and in improving its adherence to steel as well as the resistance to alkali. At 250°C, the peak of curve reached around 3 Hz; beyond that, it gradually declined as the frequency was shifted to a lower site. The Rp value between 10^{-2} and 10^{-1} Hz was ~ 4.0×10 ohm-cm^2, which was as much as three and two orders of magnitude lower than that of 200°- and 150°C-baked coatings, respectively, meaning that baking at 250°C significantly increased the extent of ionic conductivity through the coating. The increased ionic conductivity appears to be associated with the generation of numerous fissures in the coating brought about by its extended oxidation, thereby promoting the uptake of electrolyte by coating. However, no cathodic delamination was observed, manifesting that like the 200°C coating, it adhered well to the steel, and also it showed no signs of alkali dissolution at the cathodic corrosion site of steel.

Figure 11 depicts the Bode-plot curves for the $Ce(OH)_3$- and Ce_2O_3-filled PAAMPA coatings. The curve's feature for the 150°C coating attributed to the $Ce(OH)_3$-filled PAAMPA polymer clearly demonstrated that there was no cathodic delamination. The coating had a Rp value of 1.8×10^5 ohm-cm^2, which is equivalent to an increase of nearly one order of magnitude, compared with that of the PAPS coating at the same temperature. Thus, the $Ce(OH)_3$/PAAMPA coating protected the steel against corrosion far better than did the PAPS coating. This coating offered the following three advanced properties: (1) Increased densification; (2) improved adherence to steel; and, (3) insusceptibility to alkali dissolution. The further improvement in these properties can be seen in the Ce_2O_3-filled PAAMPA at 200°C. In fact, the Rp value rose to 1.8×10^5 ohm-cm^2, leading to a minimum uptake of electrolytes by the coating along with its great performance in protecting the steel against corrosion. Again, the increase in the Rp value is due to the incorporation of an additional polysiloxane network structure yielded by the condensation between the non-reacted silanol groups remaining in the original film formed at 150°C. At 250°C, its curve's feature closely resembled that of the PAPS coating at the same temperature because of the presence of copious fissures in the coating.

Although the corrosion-preventing performance of Ce_2O_3-filled PAAMPA coating was far better than that of the PAPS coating, one intriguing question still remained unanswered: What is the specific role of Ce_2O_3 in inhibiting the corrosion of steel? In trying to respond to this, we deposited thin Ce_2O_3-filled PAAMPA film on the steel's surface. This thin film was prepared by dipping-withdrawing a steel panel in a 1 wt% Ce acetate/APST solution made by diluting the original 27.2wt% Ce acetate/APST precursor solution (24.3wt% APST, 2.9wt% Ce acetate, and 72.9wt% D.I. water) with the D.I. water, followed by baking it at 200°C. The thickness of deposited film was estimated by XPS. The XPS survey spectrum (not shown) of this film showed the presence of Fe atom attributed to the underlying steel substrate coexisting with the PAAMPS- and Ce_2O_3- related atoms, such as C, O, N, Ce, and Si. Since the penetration depth of the photoelectrons was ~ 5 nm, the estimated thickness of this film was less than 5 nm. Also,

a nanoscale thickness PAPS film used as the control was similarly deposited on the steel's surface. We then conducted DC electrochemical polarization test in an aerated 0.5 M NaCl solution at 25°C for these thin film-covered steel panels. Figure 12 depicts the typical cathodic-anodic polarization curves plotting the polarization voltage, E, versus current density, A/cm^2, for the PAPS- and Ce_2O_3/PAAMPS-coated steel panels as well as the uncoated bare steel as the reference. The shape of the curves shows the transition from cathodic polarization at the onset of the most negative potential to the anodic polarization curves at the end of positive potential. The potential axis at the transition point from cathodic to anodic curves is normalized as the corrosion potential, E_{corr}. When compared with the PAPS-coated panel, there are two noticeable differences in the curves' features for the Ce_2O_3/PAAMPA-coated panel: One was a shift in the E_{corr} value to a more positive site; and, the other was a conspicuous reduction of cathodic current density (A/cm^2) at the beginning of cathodic curve. Difference (1) directly reflects the extent of coverage of the coating over the entire steel surface; namely, good coverage by a continuous void-free densified coating layer is responsible for moving the E_{corr} value to a less negative site. Hence, the resulting shift of E_{corr} to a positive site demonstrated that the Ce_2O_3/PAAMPA coating had a better coverage and a denser structure with a minimum number of voids, compared with that of the PAPS coating. However, there was no experimental evidence to tell us whether the densified coating was due to the Ce_2O_3 dispersed in the PAAMPA matrix, or to the PAAMPA itself, or both. Nevertheless, this finding strongly supported the results from the EIS study. For difference (2), a low value of cathodic current density signifies a retardation of the cathodic reaction at the corrosion site of steel, particularly of the oxygen reduction reaction, $2H_2O + O_2 + 4e^- \rightarrow 4OH^-$. Hence, the Ce_2O_3 /PAAMPA coating on the steel's surfaces inhibited this reaction, which leads to the corrosion of steel. Therefore, we can conclude that a retardation of the cathodic oxygen reduction reaction not only results from good adherence of the PAAMPA matrix to the steel's surface, but also is due to the Ce_2O_3 formed by the *in-situ* conversion of Ce acetate in the coating. If this interpretation is valid, the Ce_2O_3 precipitated on the steel's surfaces might act as a passive oxide film. We assumed that

nanometer-sized Ce_2O_3 particles formed in the thin film of < 5 nm, and so this coating assembled at 200°C was comprised of nanoscale Ce_2O_3 particles as the filler in the PAAMPA matrix. In the other words, this type of the coating can be expressed in terms of a self-assembled nanocomposite coating because of the nanoscale fillers that were developed during the conversion of the precursor solution into a nanoscale thick solid film and were dispersed in the polymer matrix. It is possible to assume that nanoscale $Ce(OH)_3$ particles were formed in the PAAMPA at 150°C. However, no further study was made to identify the size of the Ce particles dispersed in the ~ 3.5 μm thick composite coating.

On the basis of these polarization curves, we determined the absolute corrosion rates of steel, expressed in the conventional engineering units of milli-inches per year (mpy). The Eq. (1) proposed by Sterm and Geary[8], was used in the first step:

$$I_{corr} = \beta_a \cdot \beta_c / 2.303(\beta_a + \beta_c)R_p \quad (1)$$

where I_{corr} is the corrosion current density in A/cm^2, β_a and β_c having the units of V/decade of current refer to the anodic and cathodic Tafel slopes, respectively, which were obtained from the log I vs. E plots encompassing both anodic and cathodic regions, and R_p is the polarization resistance which was determined from the corrosion potential, E_{corr}. When I_{corr} was computed through Eq. (1), the corrosion rate (mpy) can be obtained from the following expression:

$$\text{Corrosion rate} = 0.13\, I_{corr}(EW)/d \quad (2)$$

where EW is the equivalent weight of the corroding species in g, and d is the density of the corroding species in g/cm^3.

Table 2 gives the I_{corr} and corrosion rate from this Tafel calculation for steel panels covered with nanoscale thick films of PAPS and Ce_2O_3/PAAMPA nanocomposite. The corrosion rate of the steel for the PAPS coating was 3.714 mpy accompanying I_{corr} of 8.125 x 10^{-6} A/cm^2. These values were as much as 29 % lower than those of the uncoated bare steel, suggesting that although the thickness of the PAPS coating is less than 5 nm, it reduced the rate of the corrosion of the steel. The nanocomposite coating further lowered the corrosion rate and the I_{corr} value to 1.064 mpy and 2.329 x 10^{-6}

A/cm^2, thereby offering better protection. In fact, these values were equivalent to a 3.49 fold increase compared with those of the PAPS.

3.4.2. Aluminum

Figure 13 depicts the EIS Bode-plot curve for the aluminum panels coated with the PAPS polymer baked at temperatures of 150°, 200°, and 250°C. The curve from the 150°C PAPS coating showed no sign of cathodic delamination of the coating, demonstrating that the PAPS coating favorably adheres to the aluminum' s surface, compared with that on the steel's surface. Correspondingly, the Rp value of 6.1×10^4 ohm-cm^2 at 150°C was more than one order of magnitude higher than that of the PAPS-coated steel at the same temperature. Such a good adherence also was responsible for the increase in Rp value at 200°C. At 250°C, unlike the steel, the coated aluminum did not show a striking reduction of Rp value; in fact, the 4.2×10^4 ohm-cm^2 recorded only fell by one order of magnitude compared with that at 200°C, underscoring that although copious fissures were generated in the coating at 250°C, the excellent adhesion between the coating and aluminum appears to prevent a serious loss of the coating's maximum protection. As expected, enhanced protection of aluminum against corrosion was observed from the $Ce(OH)_3$- and Ce_2O_3-filled PAAMPA composite coatings. As seen in the Bode-plot curves (Figure 15), the Rp values of all the composite coatings increased one order of magnitude compared with those of the PAPS coatings.

To investigate the effectiveness of Ce_2O_3 as a passive oxide film in further heightening the corrosion-preventing performance of the composite coatings, we again conducted the DC potentiodynamic polarization test for the aluminum plates covered with 200°C-made nanoscale films (< 5 nm thick) (Figure 14). As is evident from comparing the distinctive features of the curves, the results were similar to those obtained from the steel panels coated with the same materials; the E_{corr} of the composite coating was at more positive site, with a lower cathodic current density (A/cm^2) at the starting point of cathodic curve compared with those of the PAPS coating. Again, the dispersion of Ce_2O_3 particles in the PMMAPS matrix further retarded the cathodic corrosion

reaction of aluminum possibly due to the formation of its passive film at the coating/aluminum interfacial contact zones.

Table 3 shows the results of Tafel calculation for these curves. Unlike the steel, the corrosion rate of aluminum was considerably reduced by depositing the nanoscale thick composite coating on its surface, from 1.8×10^{-1} mpy for the uncoated aluminum to 4.9×10^{-3} mpy for the coated aluminum, demonstrating that a coating of less than 5 nm thick can significantly extend the useful lifetime of aluminum. In contrast, the PAPS coating did not offer as effective as did the nanocomposite coating. In fact, PAPS reduced the corrosion rate of aluminum by less than one order of magnitude.

3.4.3. Salt-spray Resistance

To support the results from the electrochemical corrosion tests described above, we carried out salt-spray resistance tests, exposing the steel and aluminum panels coated with a 3.5 μm Ce_2O_3/PAAMPA composite in a 5 % salt-fog chamber at 35°C. The thicker coatings, ~ 7.0 μm and ~ 10.0 μm, also were tested. In preparing such thick coatings, the dipping-withdrawing-200°C baking process was repeated two and three times to build up multiple-layers on the metals. One concern in assembling the thicker coating films was the susceptibility of first composite layer's surface to fresh precursor solution. If susceptibility was poor, the second composite layer film might not only cause irregular and discontinuous coverage over the entire first layer's surface, but also might be delaminated and buckled from the first layer. However, repetition of the coating process did not have this effect.

Table 4 expresses the results as the total exposure time needed to generate rust and oxide stains on the coated steel and aluminum surfaces. For the aluminum panels, the rate of corrosion was dramatically reduced by depositing a $\geq$ ~ 3.5 μm composite on it, strongly verifying that the coating's efficacy for this metal was much greater than that of steel. An incredible lengthening of its useful lifetime to more than 1800 hours was observed with these thick coatings. In contrast, the length of useful lifetime of steel

depended on the coating's thickness; with ~ 10 μm layer, its lifetime was extended by as much as 800 hours, which is ~ 790 hours longer than that of the uncoated bare steel.

4. Conclusions

Self-assembly composite material consisting of $Ce(OH)_3$ particles as the fillers and poly-acetamide-acetoxyl methyl-propylsiloxane (PAAMPS) as the polymeric matrix was synthesized through three spontaneous reactions, condensation, amidation, and acetoxylation, between the Ce acetate dopant and aminopropylsilane triol (APST) as the film-forming precursor aqueous solution at 150°C. The condensation reaction between the silanol, SiOH, groups within the APST led to the assemblage of the siloxane, Si-O-Si, linkages in the polypropylsiloxane polymer network structure. The amidating reaction between Ce acetate and amine, NH_2, group in APST provided the formation of the acetamide moiety as the end reaction product in the polymer network's structure and the $Ce(OH)_3$ nanofiller as byproduct. The acetoxylation reaction between Ce acetate and silanol group introduced the acetoxyl methyl moiety and $Ce(OH)_3$ into the network structure. When the 150°C-made PAAMPA composite was baked at 200°C, the *in-situ* phase transformation of $Ce(OH)_3$ into Ce_2O_3 took placed in the PAAMPA polymer. However, a further increased temperature to 250°C caused an undesirable oxidation degradation of the Si-joined propyl groups in the PAAMPS, yielding three oxidative derivatives, aldehyde, ketone, and carboxylic acid, brought about by the rupture of the bond between Si and C.

Using the dipping-withdraw-baking coating process, this composite material was deposited on the surfaces of carbon steel and aluminum substrates. The coatings made at 150° and 200°C displayed a good film-forming performance, reflecting the presence of a continuous, fissure-free barrier layer over these substrate surfaces. However, baking at 250°C resulted in a later that was no longer as effective a corrosion-preventing barrier as were the 150° and 200°C coatings because of the generation of copious fissures in the coating caused by oxidation. A 200°C-made coating of ~ 3.5 μm thick displayed better performance in protecting both the metals against NaCl-induced corrosion, compared

with that of the 150°C-made one. There were three reasons to improve the corrosion protection for 200°C-made coating: One was to ensure the coverage of more densified barrier layer to prevent electrolytes moving through the coating; second was to lower the susceptibility of coating's surface to moisture; and, the third referred to the formation of interfacial Ce_2O_3 passive film coexisting with the PAAMPA over the substrates' surfaces, retarding the cathodic oxygen reduction reaction at the corrosion site of the metals. The densified layer (the first reason) was formed by the promotion at 200°C of the condensation reaction between the non-reacted silanol groups remaining in the 150°C coating. Another important factor governing corrosion prevention was the magnitude of wettability of the precursor solution over the substrates' surfaces along with the extent of adherence of the coatings to the substrates. For the former factor, the wettability of aluminum's surface by precursor solution was much higher than that of the steel's surface. Correspondingly, the composite favorably adhered to aluminum, but not to steel. In fact, the combination of all these factors contributed to extending remarkably the useful lifetime of aluminum. With an ~ 10.0 μm thick coating film, the useful lifetime of aluminum in a 5 % salt-fog chamber at 35°C was considerably prolonged from ~ 40 hours for uncoated aluminum to more than 1800 hours. In contrast, the length of lifetime of the steel was extended only by 800 hours.

References

1. C.F. Kutscher and D. Dostenaro, Geotherm. Resour. Counc. Trans. 26 (2002) 775.
2. D.B. Jung, "Brine Enhanced Air Cooling, Final Technical Report, "DOE Golden Field Office Technical Report DOE/DE-FC36-99GO10441, Dec. 31, 2001.
3. K. Gawlik and T. Sugama, Geotherm. Resour. Counc. Trans. 26 (2002) 657.
4. T. Sugama and K. Gawlik, Recent Rec. Devel. Mat. Sci. 4 (2003) 695.
5. F. Mansfeld, C.B. Breslin, A. Pardo and F.J. Perez, Surf. Coat. Tech. 90 (1997) 224.

6. M. Balasubramania, C.A. Melendres and A.N. Mansour, Thin Solid Films 347 (1999) 178.
7. M. Dabala, L. Armelao, A. Buchberger and I. Calliari, Appl. Surf. Sci. 172 (2001) 312.
8. W.G. Fahrenholtz, M.J. O'Keefe, H. Zhou and J.T. Grant, Surf. Coat. Tech. 155 (2002) 208.
9. M.A. Arenas, A. Conde and J.J. de Damborenea, Corrosion Sci. 44 (2002) 511.
10. X. Yu and C. Cao, Thin Solid Films 423 (2003) 252.
11. B.F. Rivera, B.Y. Johnson, M.J. O'Keefe and W.G. Fahrenholz, Surf. Coat. Tech. 176 (2004) 349.
12. T. Sugama and S. Milian-Jimenez, J. Mater. Sci. 34 (1999) 2003.
13. G.J. Su, N.F. Borelli and A.R. Miller, Chem. Glasses, 3 (1962).
14. P.J. Launer, in "Silicon Compounds Register and Review" (Petrarch Systems, Pennsylvania 1987) pp 69-72.
15. L.J. Bellamy, in "The infra-red Spectra of Complex Molecules" (Chapman & Hall, London, 1975) p. 231.
16. K. Nakanish and P.H. Solomon, in "Infrared Absorption Spectroscopy" (Hoden-Day, Inc, San Fransisco, 1977) p. 15.
17. L.S. Kasten, J.T. Garnt, N. Grebasch, N. Voevodin, F.E. Arnold and M.S. Donley, Surf. Coat. Tech. 140 (2001) 11.
18. D. Barreca, G.A. Battiston, R. Berbasi and E. Tondello, Surf. Sci. Spect. 7 (2000) 297.

Table 1. Some properties of Ce acetate-modified and unmodified APST precursor solutions.

Ce acetate, wt%	**pH**	**Surface tension, dynes/cm**	**Contact angle, degrees**	
			Steel	**Aluminum**
0	10.95	55.0	40.8	26.9
3	10.54	56.2	42.3	29.2

Table 2. Tafel analyses for potentiodynamic polarization diagrams of uncoated bare steel and, PAPS- and Ce_2O_3/PAAMPA-coated steel panels.

Coating	**E_{corr} (I=0), (V)**	**β_a, (V/decade)**	**β_c, (V/decade)**	**I_{corr}, (A/cm^2)**	**Corrosion rate, (mpy)***
Bare steel	-0.7191	0.04135	0.4184	1.150×10^{-5}	5.257
PAPS	-0.6540	0.0619	6.955	8.125×10^{-6}	3.714
Ce_2O_3/PAAMPA	-0.6247	0.0522	0.7335	2.329×10^{-6}	1.064

* mpy: milli-inches per year

Table 3. Tafel analyses for potentiodynamic polarization diagrams of uncoated aluminum and PAPS- and Ce_2O_3/PAAMPA-coated aluminum panels.

Coating	**E_{corr} (I=0), (V)**	**β_a, (V/decade)**	**β_c, (V/decade)**	**I_{corr}, (A/cm^2)**	**Corrosion rate, (mpy)***
Uncoated aluminum	-0.6268	0.1442	0.4461	4.213×10^{-5}	1.8×10^{-1}
PAPS	-1.039	1.182×10^{3}	0.3467	1.588×10^{-5}	6.8×10^{-2}
Ce_2O_3/PAAMPA	-0.6621	0.5431	0.1683	1.155×10^{-8}	4.9×10^{-3}

* mpy: milli-inches per year

Table 4. Salt-spray resistance tests for PAPS- and Ce_2O_3/PAAMPA composite-coated steel and aluminum panels.

Substrate	**Coating**	**Thickness of coating, μm**	**Salt-spray resistance, hours**
Steel	Uncoated	-	~ 10
Steel	Ce_2O_3/PAAMPA	~ 3.5	~ 168
Steel	Ce_2O_3/PAAMPA	~ 7.0	~672
Steel	Ce_2O_3/PAAMPA	~ 10.0	~ 800
Aluminum	Uncoated	-	~ 40
Aluminum	Ce_2O_3/PAAMPA	~ 3.5	> 1800
Aluminum	Ce_2O_3/PAAMPA	~ 7.0	> 1800
Aluminum	Ce_2O_3/PAAMPA	~ 10.0	> 1800

Figure captions

Fig. 1. FT-IR spectra for polymeric films derived from APST precursor solution at 150°, 200°, and 250°C.

Fig. 2. Changes in XPS O/C atomic ratio on the PAPS film's surface as function of temperature.

Fig. 3. XPS C1s core-level spectra for PAPS films' surfaces baked at 150°, 200°, and 250°C.

Fig. 4. Comparison of FT-IR spectral features for polymeric films derived from the Ce acetate-modified APST precursor solution at 150°, 200°, and 250°C.

Fig. 5. FT-IR spectra for Ce hydroxide and Ce oxide reference samples.

Fig. 6. XPS Ce3d core-level excitation for PAAMPA composite film's surface.

Fig. 7. TGA curves for PAAMPA composite films made at temperature of 150°, 200°, and 250°C.

Fig. 8. SEM images of PAAMPA composite coatings' surfaces made at 150°, 200°, and 250°C.

Fig. 9. Changes in contact angle of water on the surfaces of PAPS coating and PAAMPA composite coating as a function of baking temperature.

Fig. 10. EIS spectra for steel plates coated with 150°-, 200°-, and 250°C-baked PAPS polymers.

Fig. 11. Comparison of EIS curves for steel plates covered with 150°-, 200°-, and 250°C-baked PAAMPA composite polymers.

Fig. 12. Polarization curves for uncoated steel (a), and 200°C PAPS (b)- and 200°C PAAMPA composite (c)-coated steel plates.

Fig. 13. EIS spectra for aluminum plates coated with 150°-, 200°-, and 250°C-baked PAPS polymers.

Fig. 14. EIS spectra for aluminum plates covered with 150°-, 200°-, and 250°C-baked PAAMPA composite coatings.

Fig. 15. Polarization curves for uncoated aluminum (a), and 200°C PAPS (b)- and 200°C PAAMPA composite (c)-coated aluminum plates.

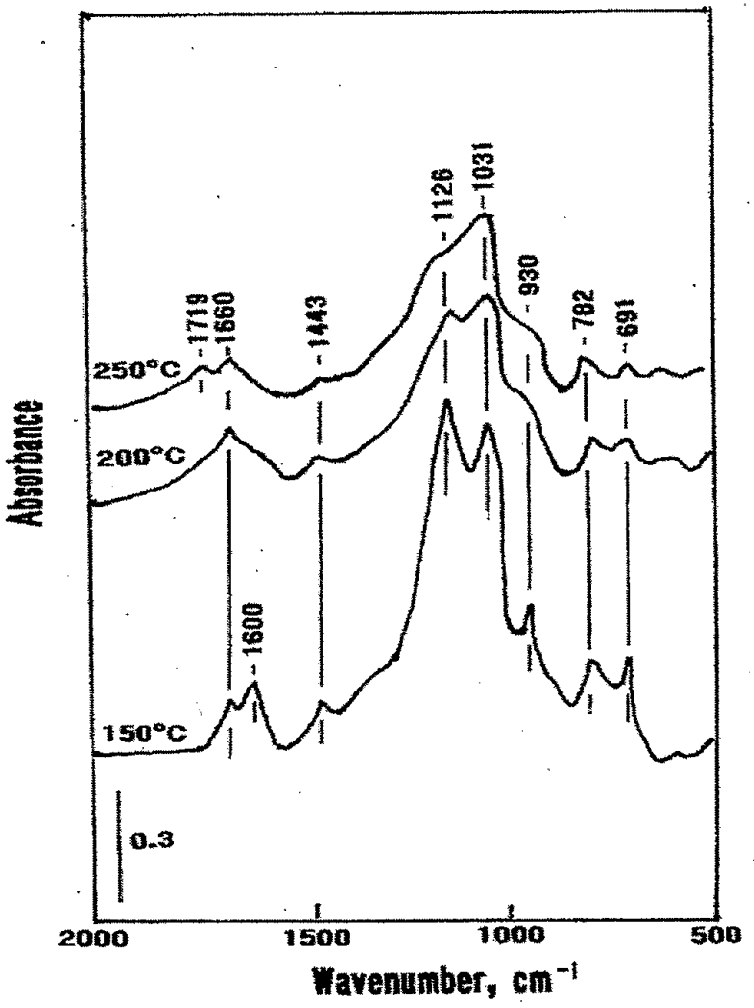

Fig. 1. FT-IR spectra for polymeric films derived from APST precursor solution at 150°, 200°, and 250°C.

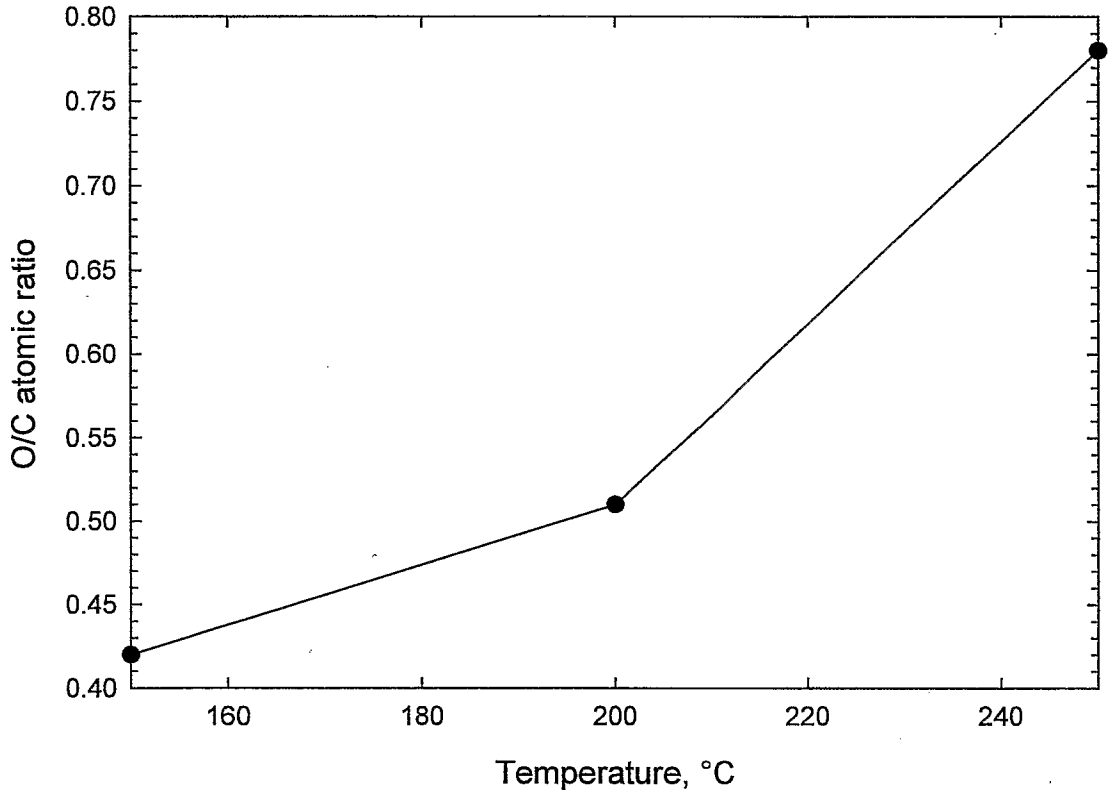

Fig. 2. Changes in XPS O/C atomic ratio on the PAPS film's surface as function of temperature.

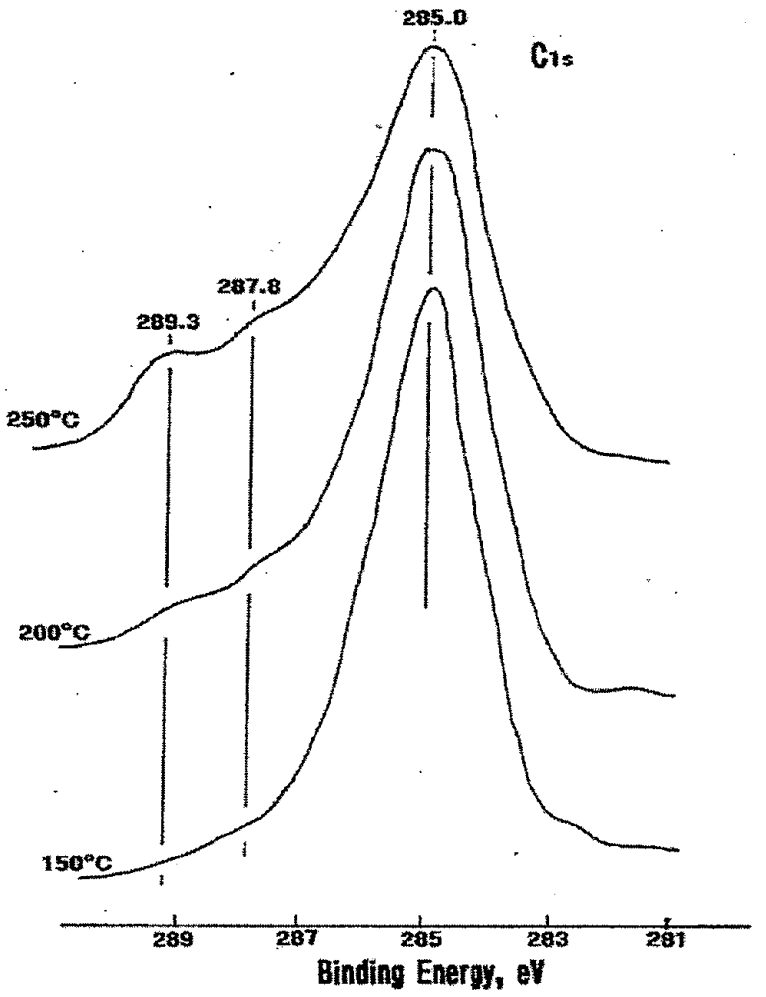

Fig. 3. XPS C_{1s} core-level spectra for PAPS films' surfaces baked at 150°, 200°, and 250°C.

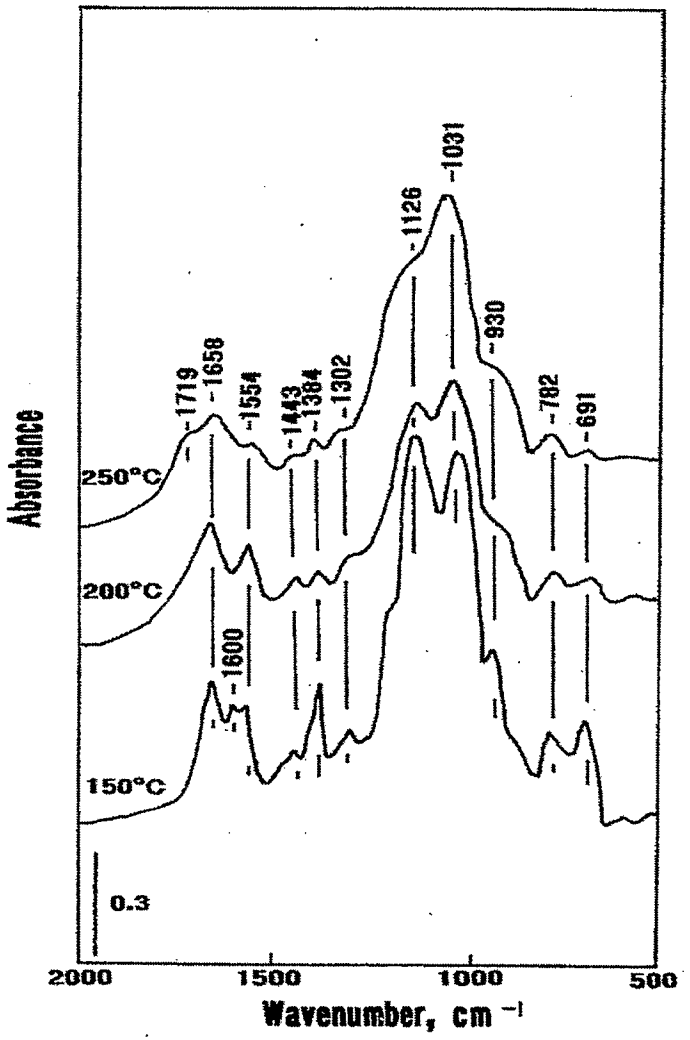

Fig. 4. Comparison of FT-IR spectral features for polymeric films derived from the Ce acetate-modified APST precursor solution at 150°, 200°, and 250°C.

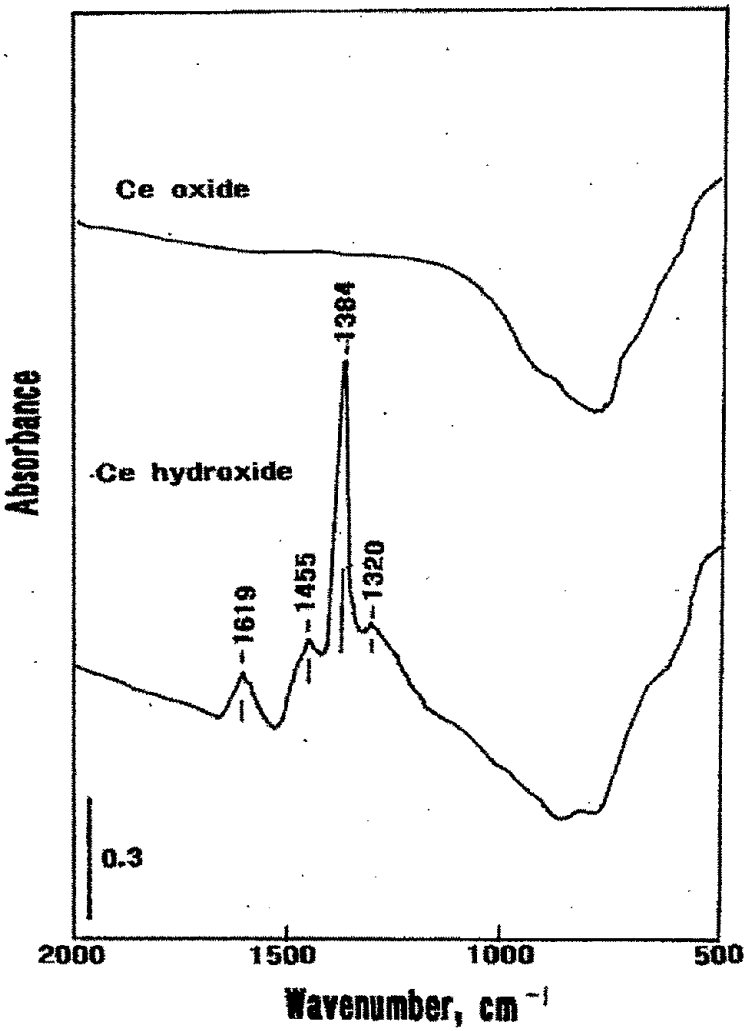

Fig. 5. FT-IR spectra for Ce hydroxide and Ce oxide reference samples.

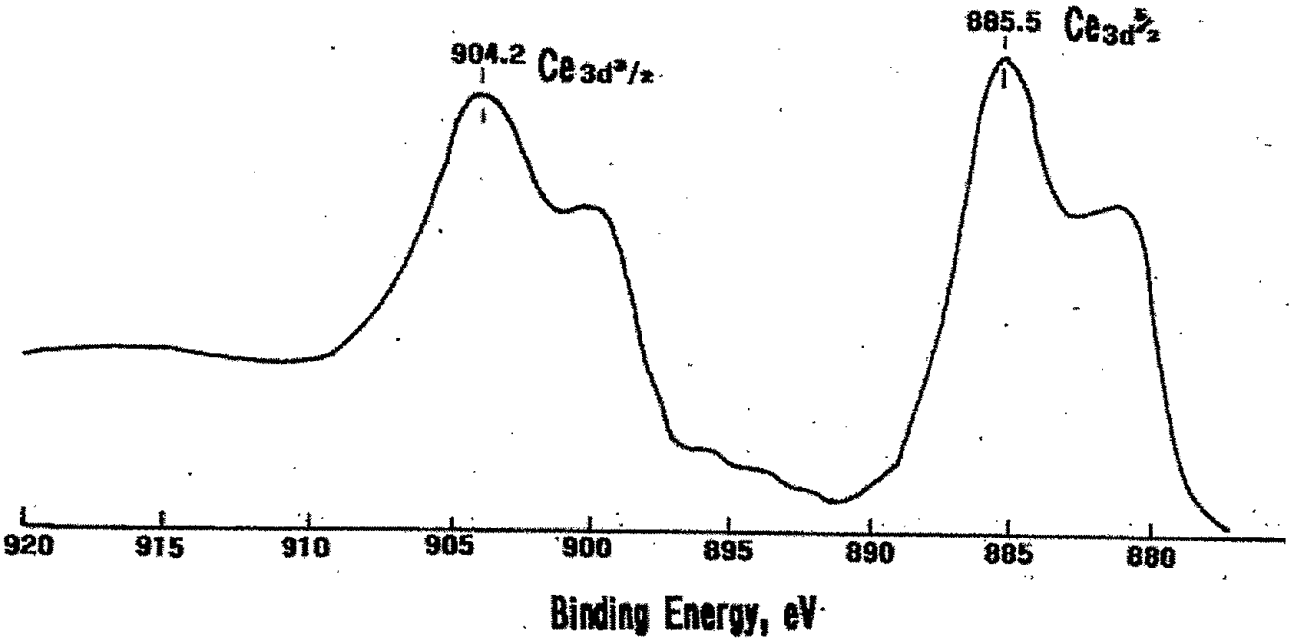

Fig. 6. XPS Ce_{3d} core-level excitation for PAAMPA composite film's surface.

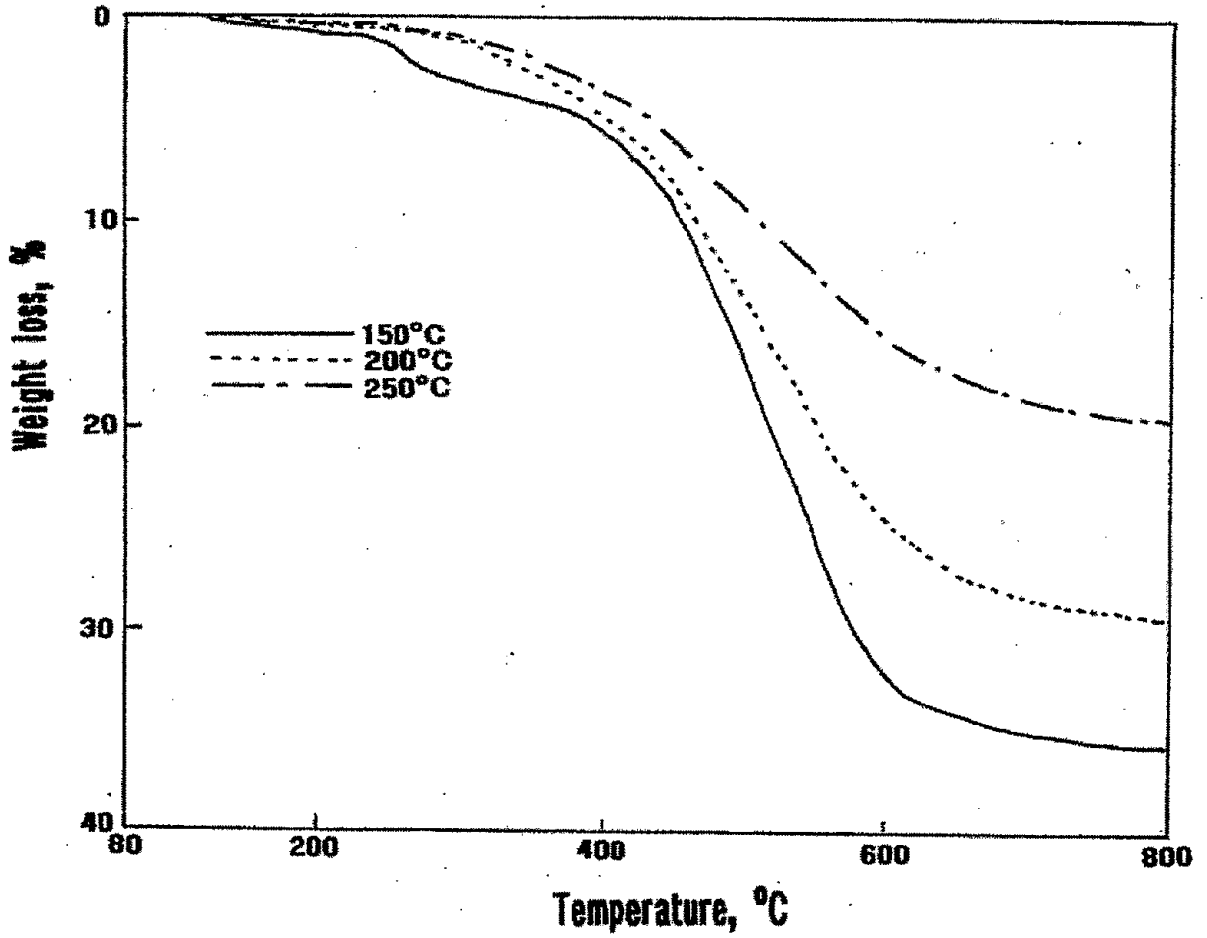

Fig. 7. TGA curves for PAAMPA composite films made at temperature of 150°, 200°, and 250°C.

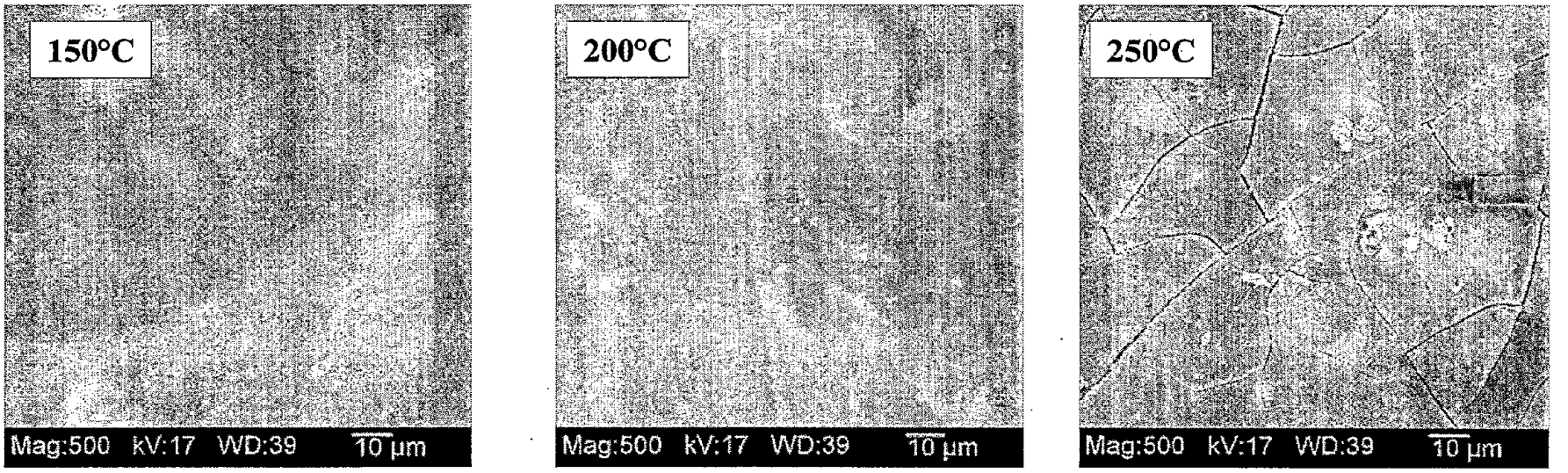

Fig. 8. SEM images of PAAMPA composite coatings' surfaces made at 150°, 200°, and 250°C.

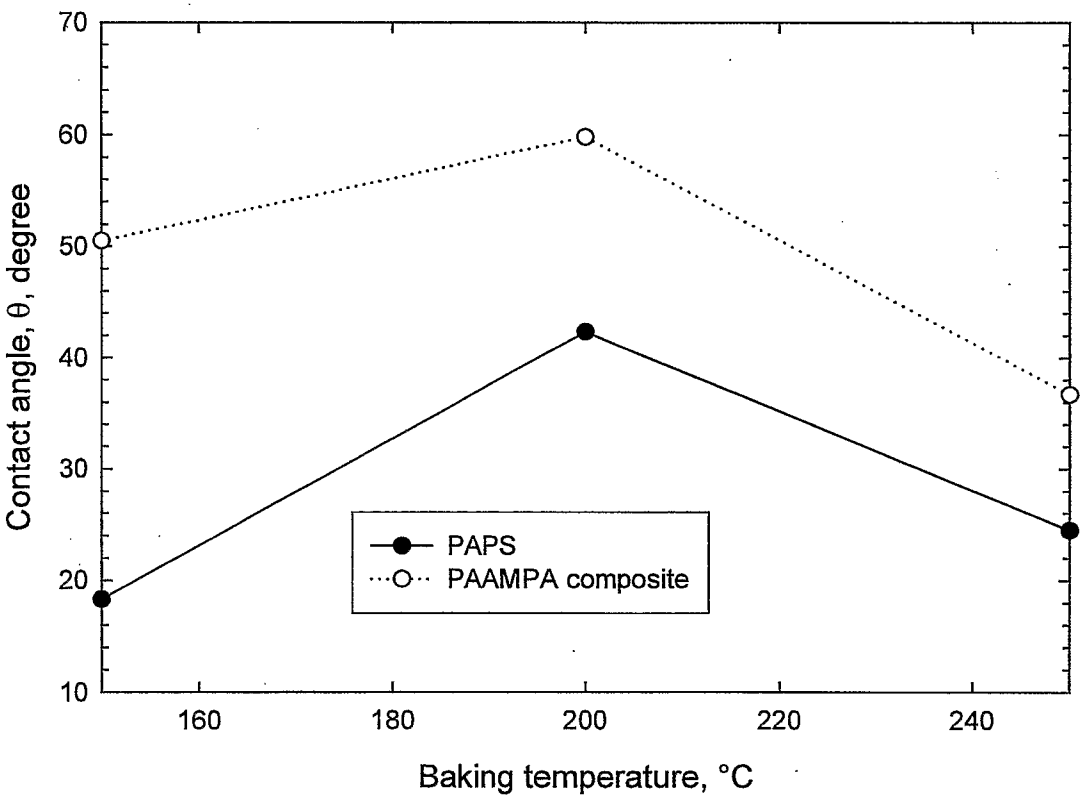

Fig. 9. Changes in contact angle of water on the surfaces of PAPS coating and PAAMPA composite coating as a function of baking temperature.

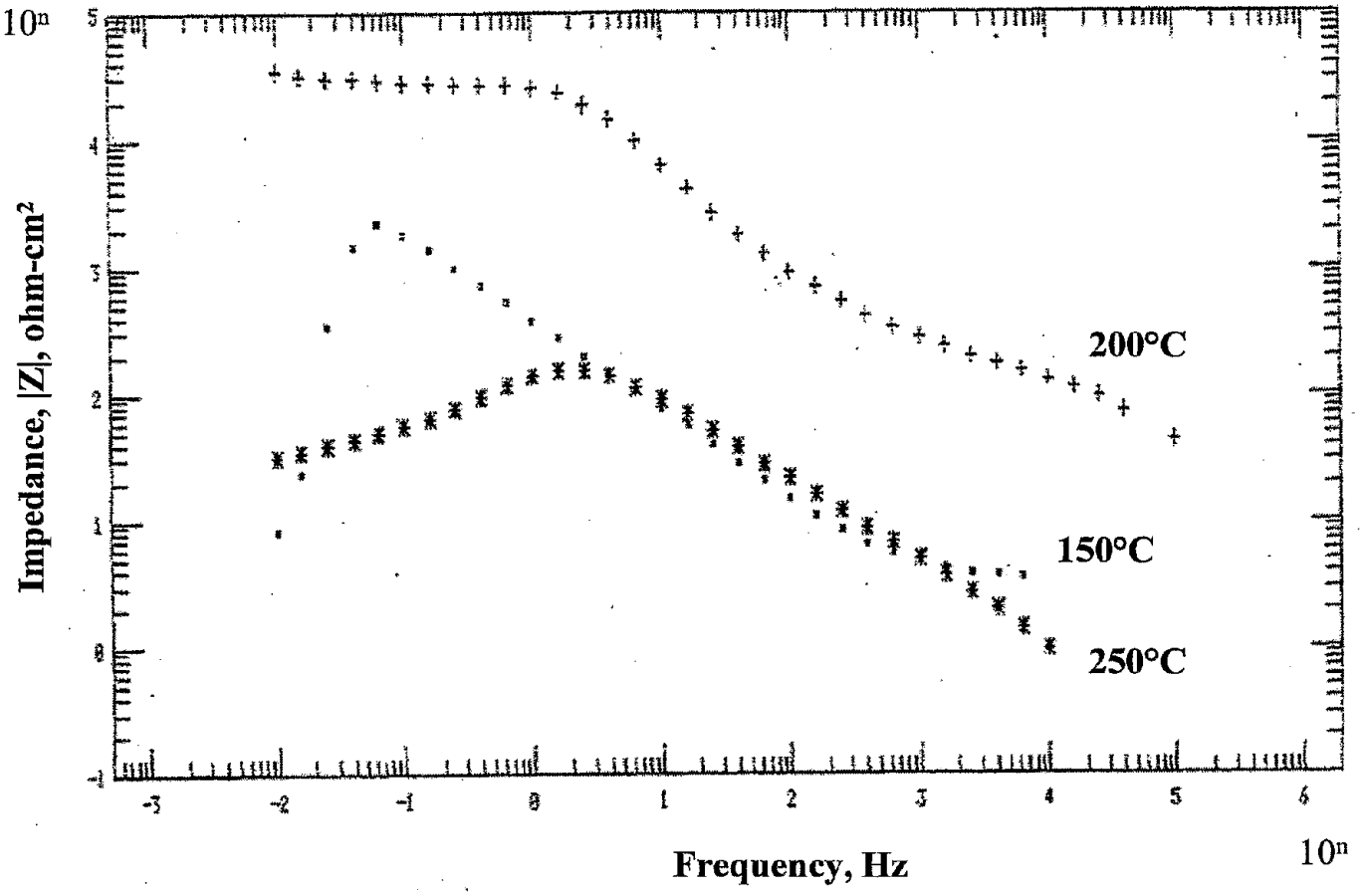

Fig. 10. EIS spectra for steel plates coated with 150°-, 200°-, and 250°C-baked PAPS polymers.

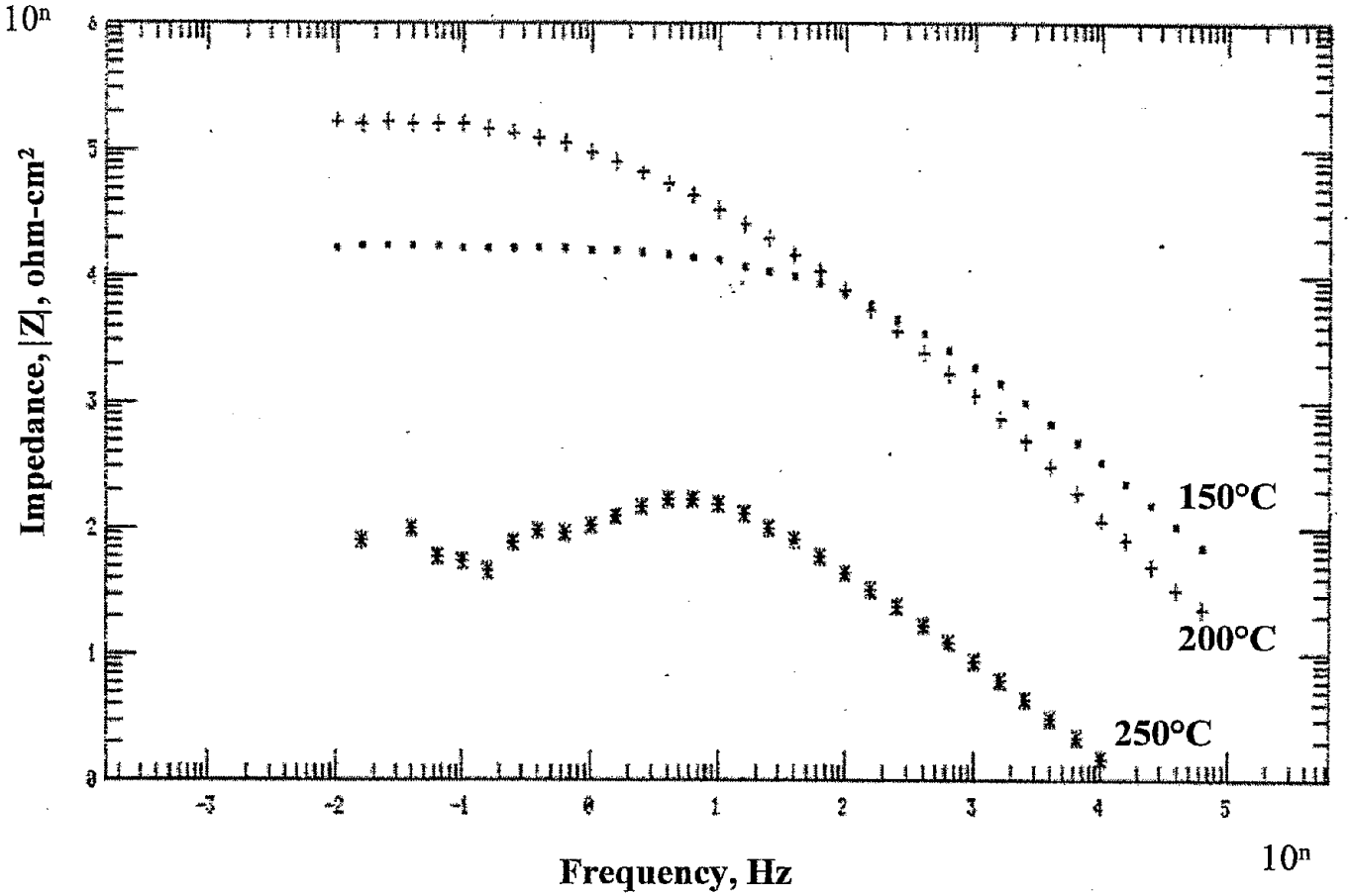

Fig. 11. Comparison of EIS curves for steel plates covered with 150°-, 200°-, and 250°C-baked PAAMPA composite polymers.

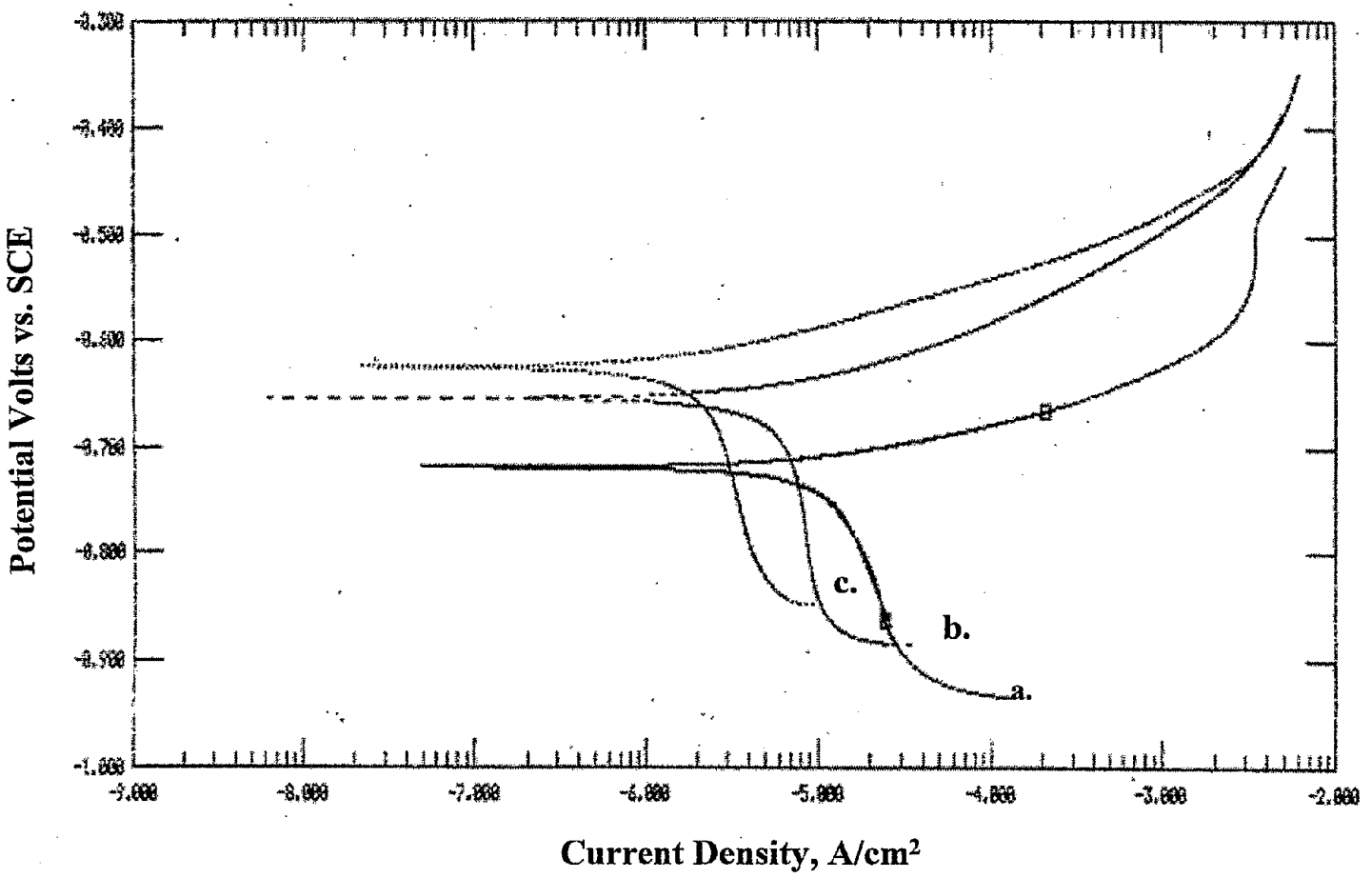

Fig. 12. Polarization curves for uncoated steel (a), and 200°C PAPS (b)- and 200°C PAAMPA composite (c)-coated steel plates.

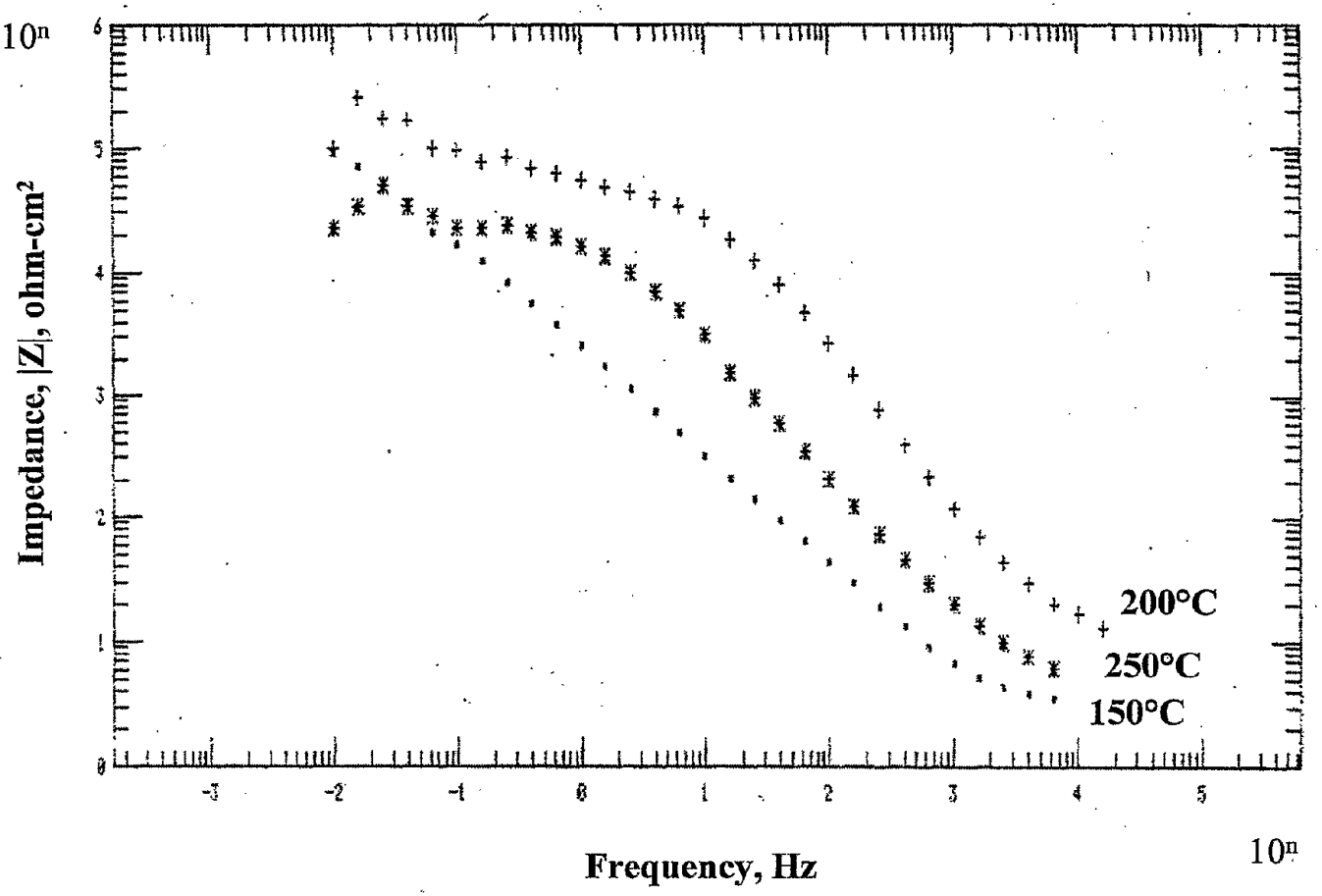

Fig. 13. EIS spectra for aluminum plates coated with 150°-, 200°-, and 250°C-baked PAPS polymers.

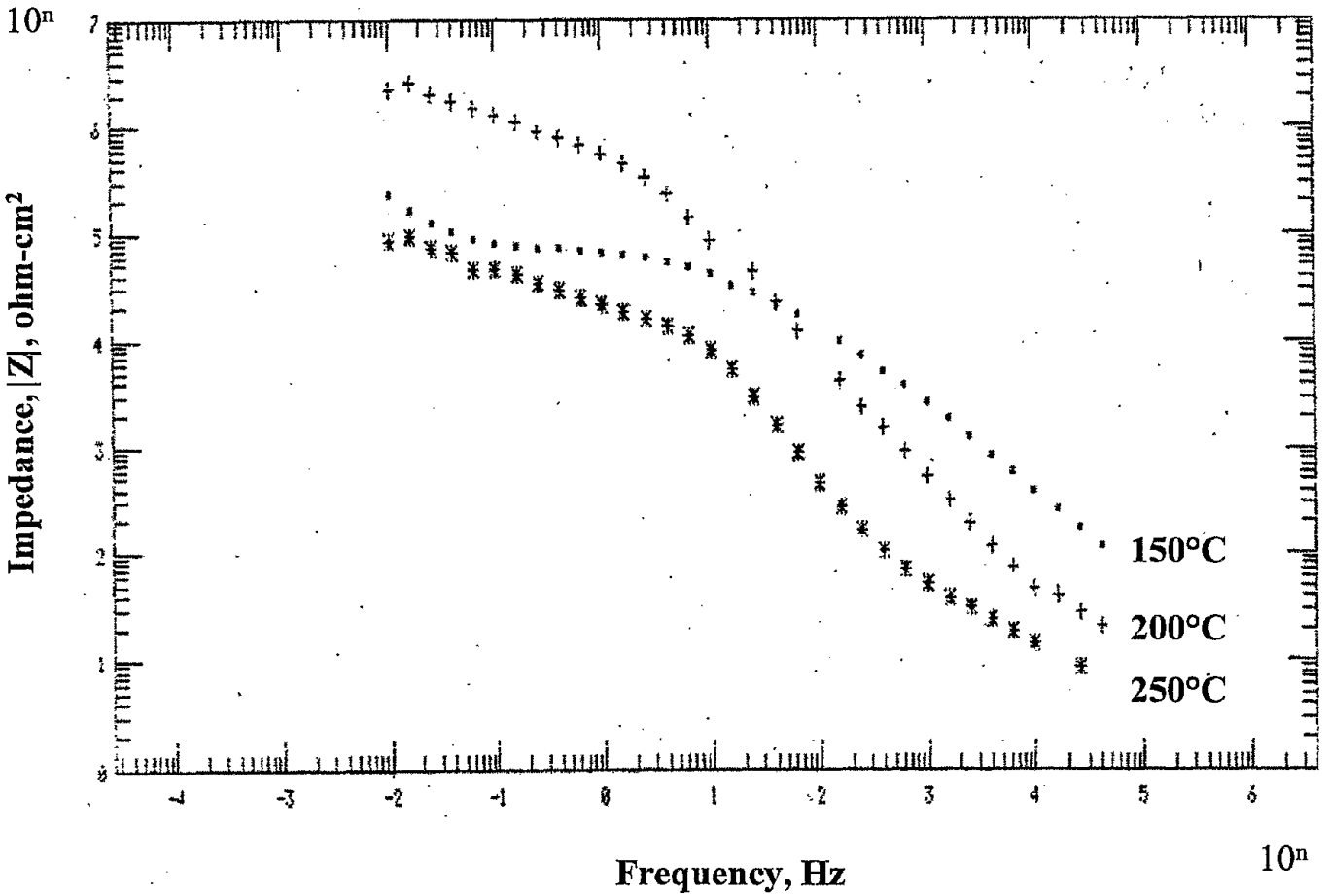

Fig. 14. EIS spectra for aluminum plates covered with 150°-, 200°-, and 250°C-baked PAAMPA composite coatings.

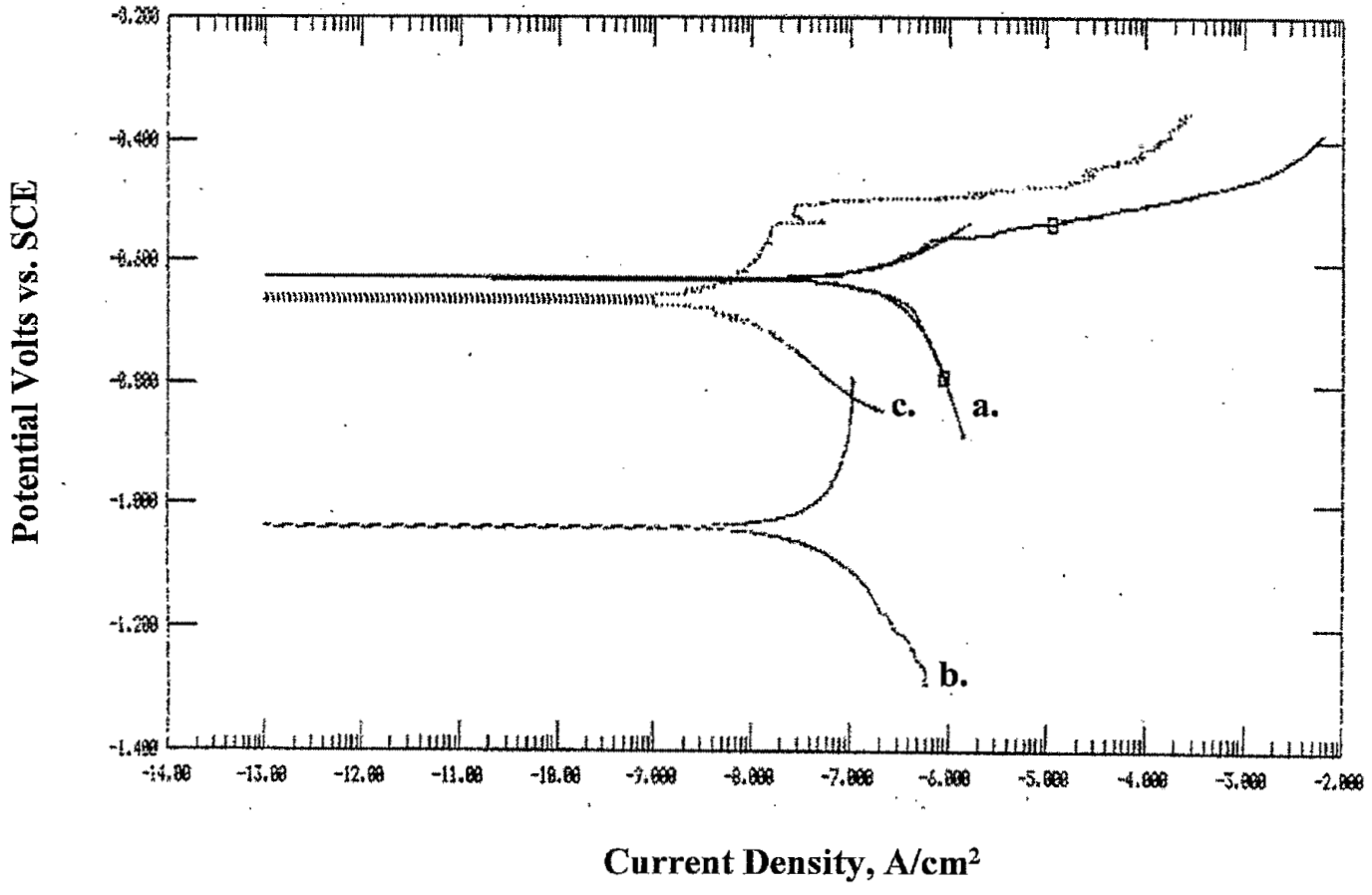

Fig. 15. Polarization curves for uncoated aluminum (a), and 200°C PAPS (b)- and 200°C PAAMPA composite (c)-coated aluminum plates.